



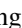
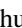


High-pressure synthesis, crystal structure, and properties of iron-based spin-chain compound $\text{Ba}_9\text{Fe}_3\text{Se}_{15}$

Jun Zhang ^{1,*}, Alexander C. Komarek,^{2,*} Meiling Jin,^{3,*} Xiancheng Wang ^{1,4,†}, Yating Jia,¹ Jianfa Zhao,^{1,5} Wenmin Li,¹ Zhiwei Hu,² Wei Peng ², Xiao Wang,² Liu Hao Tjeng ², Zheng Deng ¹, Runze Yu,¹ Shaomin Feng,¹ Sijia Zhang,¹ Min Liu,^{1,4} Yi-feng Yang,^{1,4,5} Hong-ji Lin,⁶ Chien-Te Chen,⁶ Xiaodong Li ⁷, Jinlong Zhu,^{3,‡} and Changqing Jin^{1,4,5,§}

¹Beijing National Laboratory for Condensed Matter Physics, Institute of Physics, Chinese Academy of Sciences, Beijing 100190, China

²Max Plank Institute for Chemical Physics of Solids, Nöthnitzer Straße 40, D-01187 Dresden, Germany

³Department of Physics, Southern University of Science and Technology, Shenzhen 518055, China

⁴School of Physics, University of Chinese Academy of Sciences, Beijing 100190, China

⁵Songshan Lake Materials Laboratory, Dongguan, Guangdong 523808, China

⁶National Synchrotron Radiation Research Center (NSRRC), 101 Hsin-Ann Road, Hsinchu 30076, Taiwan

⁷Institute of High Energy Physics, Chinese Academy of Sciences, Beijing 100049, China



(Received 10 February 2021; accepted 21 April 2021; published 28 May 2021)

We report the synthesis of a quasi-one-dimensional (1D) iron selenide $\text{Ba}_9\text{Fe}_3\text{Se}_{15}$. It was synthesized at high temperature and high pressure of 5.5 GPa and systematically studied via structural, magnetic, and transport measurements at both ambient and high pressure. $\text{Ba}_9\text{Fe}_3\text{Se}_{15}$ crystallizes in a monoclinic structure and consists of face-sharing FeSe_6 octahedral chains running in c -direction. It shows a sizable unquenched orbital moment and undergoes a ferromagnetic-like phase transition at 14 K. At ambient pressure, $\text{Ba}_9\text{Fe}_3\text{Se}_{15}$ exhibits an insulating behavior with a band gap of ~ 460 meV. Under high pressure, a complete metallization occurs at ~ 29 GPa, which is accompanied by a spin state crossover from high-spin to low-spin state.

DOI: [10.1103/PhysRevMaterials.5.054606](https://doi.org/10.1103/PhysRevMaterials.5.054606)

I. INTRODUCTION

The iron selenide compounds have attracted much attention because of the superconductivity (SC) reported in the iron-based superconductors (IBSs) [1–5]. FeSe is a simple layered superconductor where the antiferromagnetic-type [FeSe] layers are bonded with Van der Waals force. The bulk FeSe exhibits SC < 9 K, while the SC transition temperature T_c can be enhanced by introducing charge carriers into the system either via the interface effect between the monolayer of FeSe and the SrTiO_3 substrate or intercalating alkaline earth metals into the FeSe layers. Although FeSe does not possess long-range magnetic ordering, the stripe spin fluctuation was evidenced to interplay with SC in FeSe, which reveals that SC is driven by the spin fluctuation. Besides the layered iron selenide superconductors, it is inspired that the SCs were observed in the spin-ladder iron chalcogenides BaFe_2S_3 and BaFe_2Se_3 under high pressure [6–8]. The crystal structure of these iron chalcogenides consists of spin ladders along the c axis formed by the edge-sharing FeS_4 (FeSe_4) tetrahedrons. BaFe_2S_3 is a Mott insulator with stripe-type antiferromagnetic (AFM) ordering < 120 K. By applying pressure, SC with $T_c \sim 24$ K was induced above the critical pressure of 10 GPa, before which the AFM ordering was suppressed [6]. While BaFe_2Se_3 undergoes a block-type AFM structure at $T_N = 256$ K [9]. The SC ($T_c \sim 11$ K) emerges after the local magnetic moment is

decreased by pressure and is comparable with the layered IBSs [8]. It seems that SC discovered in IBSs is closely related with magnetism, although they have various AFM structures.

Based on the above results, it is interesting to look for other IBSs with quasi-one-dimensional (1D) structure. Using the high-pressure method, we have synthesized several hexagonal $\text{Hf}_5\text{Sn}_3\text{Cu}$ -anti-type materials with a general formula of A_3BX_5 , where the face-sharing BX_6 octahedral chains are separated by a large distance > 9 Å, exhibiting a strong 1D structure characteristic [10–15]. Among these quasi-1D materials, the iron telluride $\text{Ba}_9\text{Fe}_3\text{Te}_{15}$ with FeTe_6 octahedral chains was reported to display a 1D AFM behavior [15] and show pressure-induced SC with a maximum $T_c \sim 4.7$ K [16]. Here, we report the synthesis of iron selenide $\text{Ba}_9\text{Fe}_3\text{Se}_{15}$. The crystal structure was solved by a combined powder and single crystal x-ray diffraction (XRD) method. $\text{Ba}_9\text{Fe}_3\text{Se}_{15}$ crystallizes into a monoclinic structure with face-sharing FeSe_6 octahedral chains along the c axis. The magnetic susceptibility measurements suggest a ferromagnetic (FM)-like phase transition at ~ 14 K. $\text{Ba}_9\text{Fe}_3\text{Se}_{15}$ is an insulator at ambient pressure with a band gap ~ 460 meV. When applying high pressure, a complete pressure-induced metallization and a spin state transition (SST) occur simultaneously at ~ 29 GPa. The SST should be finished when $P > 36$ GPa, and no SC was observed within the experimental pressure range of 52 GPa.

*These authors contributed equally to this paper.

†Corresponding author: wangxiancheng@iphy.ac.cn

‡zhujl@sustech.edu.cn

§jin@iphy.ac.cn

II. EXPERIMENTS

$\text{Ba}_9\text{Fe}_3\text{Se}_{15}$ was synthesized by solid state reaction at high-pressure and high-temperature conditions. Lumps of Ba (Alfa,

immersed in oil, >99.2% pure), crystalline powders of Fe (Alfa, 99.998% pure), and Se (Alfa, >99.999% pure) were used as the starting materials. Initially, a precursor of BaSe was prepared by heating the mixture of Ba blocks and Se powder in an evacuated quartz tube at 600 °C for 10 h. A mixture of BaSe, Fe, and Se powders with stoichiometric ratio of 3:1:2 was ground and pressed into a flake, which was then sintered at 1200 °C under 5.5 GPa for 30 min. A black polycrystalline sample of Ba₉Fe₃Se₁₅ was obtained. Small single crystals can be extracted from the polycrystalline sample.

Single-crystal XRD measurements have been performed on a Bruker D8 VENTURE single-crystal x-ray diffractometer using monochromatic Mo *K*α radiation ($\lambda = 0.71073 \text{ \AA}$) and a bent graphite monochromator for about $3\times$ intensity enhancement as well as a Photon CMOS large area detector. Here, 91 899 reflections [with 99.96% (98.09%) coverage up to $\sin \theta/\lambda = 0.9052$] have been collected up to $2\theta_{\max} = 85.52^\circ$ with a redundancy of 4.374 and an internal *R* value of 3.96%. Powder XRD measurements have been performed on a high-resolution Bruker D8 Discover A25 powder x-ray diffractometer with monochromatic Cu-*K*_{α,1} radiation.

The stoichiometry of single-crystalline Ba₉Fe₃Se₁₅ was determined by energy-dispersive x-ray spectroscopy (EDX). The direct current (DC) magnetic susceptibility was measured within a temperature range of 2–700 K using a superconducting quantum interference device. A physical property measurement system was used for measuring the resistivity under ambient pressure by a standard four-probe technique. The Mössbauer spectroscopy measurements were performed using a SEE Co. conventional constant acceleration type spectrometer in transmission geometry with an ⁵⁷Co(Rh) source at room temperature. To optimize the signal intensity, a Ba₉Fe₃Se₁₅ sample synthesized with ⁵⁷Fe was used for the Mössbauer spectroscopy measurements. Soft x-ray absorption spectroscopy (XAS) at the Fe-*L*_{2,3} edges was performed at the beamline BL11A of the National Synchrotron Radiation Research Center in Taiwan.

The *in situ* resistance measurements were conducted in a Maglab system within 2–300 K via the Van der Pauw method in diamond anvil cell (DACs) made of CuBe alloy. The diamond culet was 300 μm in diameter. A T301 stainless steel was used as the gasket; cubic BN serves as an insulating layer and NaCl fine powder as a pressure transmitting medium. The pressure was calibrated by the ruby fluorescence method. The single crystal of the Ba₉Fe₃Se₁₅ sample was crushed into small fragments, and a piece sample with dimensions of 40 × 40 × 5 μm was selected for the measurements. The details of *in situ* high-pressure experiments can be seen in the Ref. [16].

High-pressure synchrotron XRD experiments were performed at the Beijing Synchrotron Radiation Facility at room temperature with a wavelength 0.6199 Å in a symmetric DAC. Silicon oil was loaded as the pressure-transmitting medium for these experiments. The high-pressure x-ray emission spectra (XES) experiments were performed at room temperature at the 16 ID-D station of HPCAT of the Argonne National Laboratory. For the high-pressure XES experiments, Be gaskets were used as a sample chamber, and neon gas was used as a pressure-transmitting medium.

TABLE I. Atomic coordinates and isotropic displacement parameters (\AA^2) of Ba₉Fe₃Se₁₅.

Atom	<i>x</i>	<i>y</i>	<i>z</i>	<i>U</i> (eq)
Empirical formula: Ba ₉ Fe ₃ Se ₁₅				
Space group: <i>C2/c</i> (15)—monoclinic				
<i>a</i> = 16.5947(2) Å, <i>b</i> = 9.6128(1) Å, <i>c</i> = 18.6735(2) Å				
$\alpha = 90^\circ$, $\beta = 90.110(2)^\circ$, $\gamma = 90^\circ$				
<i>V</i> = 2978.82(6) Å ³ , <i>Z</i> = 2				
Goodness of fit: 1.42; <i>R</i> / <i>R</i> _w values: 4.29%/6.83%				
Atom	<i>x</i>	<i>y</i>	<i>z</i>	<i>U</i> (eq)
Ba1	0.68375 (9)	0.29790 (19)	0.08279 (8)	0.0085 (3)
Ba2	0.30719 (9)	0.3252 (2)	0.08345 (8)	0.0114 (4)
Ba3	0.00884 (12)	0.37534 (18)	0.08328 (9)	0.0117 (4)
Ba4	0.18913 (10)	0.1892 (2)	0.24974 (11)	0.0149 (5)
Ba5	0.5	0.1229 (3)	0.25	0.0122 (6)
Fe1	0	0	0	0.0197 (19)
Fe2	0.0001 (3)	0.0007 (6)	0.17043 (8)	0.0205 (10)
Se1	0.3334 (2)	0.0021 (4)	0.01606 (5)	0.0128 (4)
Se2	0.88867 (18)	0.1206 (3)	0.08253 (13)	0.0094 (7)
Se3	0.6669 (2)	0.0023 (4)	0.17336 (5)	0.0134 (5)
Se4	0.11547 (18)	0.1084 (3)	0.08324 (14)	0.0112 (7)
Se5	0.38701 (16)	0.3857 (3)	0.24968 (16)	0.0100 (7)
Se6	0	0.2288 (5)	0.25	0.0156 (11)
Se7	0.4960 (2)	0.2704 (3)	0.0834 (1)	0.0111 (7)
Se8	0.33280 (4)	−0.0007 (3)	0.15002 (4)	0.0128 (4)

III. RESULTS AND DISCUSSIONS

The synthesized Ba₉Fe₃Se₁₅ single crystals are rodlike in shape with the typical size of ~0.3 mm in length, see the inset of Fig. 1(a). The stoichiometry of single-crystalline Ba₉Fe₃Se₁₅ measured by EDX shows that the average atomic ratio of Ba:Fe:Se is 3.1(6):1.4(9)(8), which is close to the stoichiometric formula of Ba₉Fe₃Se₁₅, see Fig. 1(a).

Ba₉Fe₃Se₁₅ crystallizes in a monoclinic crystal structure that was solved within a combined powder and single-crystal XRD study and that is related to the already known structure of Ba₉Fe₃S₁₅ [17]. Powder XRD measurements clearly indicate that neither hexagonal nor crystal structures with symmetries higher than monoclinic can describe the XRD patterns of Ba₉Fe₃Se₁₅ satisfactorily, see Figs. 1(b)–1(e). The space group with highest symmetry that provides a structural model that can describe the powder and single-crystal XRD data satisfactory is *C2/c*. A Rietveld refinement of the powder XRD data that is using the positional parameters obtained by single-crystal XRD is shown in Fig. 1(f) and gives the lattice constant *a* = 16.5947 Å, *b* = 9.6128 Å, *c* = 18.6735 Å, and $\beta = 90.11^\circ$. The summary of the crystallographic data is shown in Table I. The finally obtained crystal structure based on space group *C2/c* consists of face-sharing FeSe₆ octahedral chains running along the *c* axis that are separated by Ba²⁺ ions and Se chains with a distance >9.5 Å, thus exhibiting strong 1D spin-chain structure, as seen in Fig. 1(g). There are two Fe sites in the monoclinic crystal structure of Ba₉Fe₃Se₁₅ [see Fig. 1(h)]. The distance of nearest neighbor Fe1 and Fe2 ions is 3.1825 Å, while it is 2.9717 Å for the distance of two Fe2 ions. The bond valence sums (BVSs) of both Fe sites, Fe1 and Fe2, amounts to 2.02(1), which indicates a 2+ oxidation state of the iron ions in Ba₉Fe₃Se₁₅. For the Se ions, the BVS

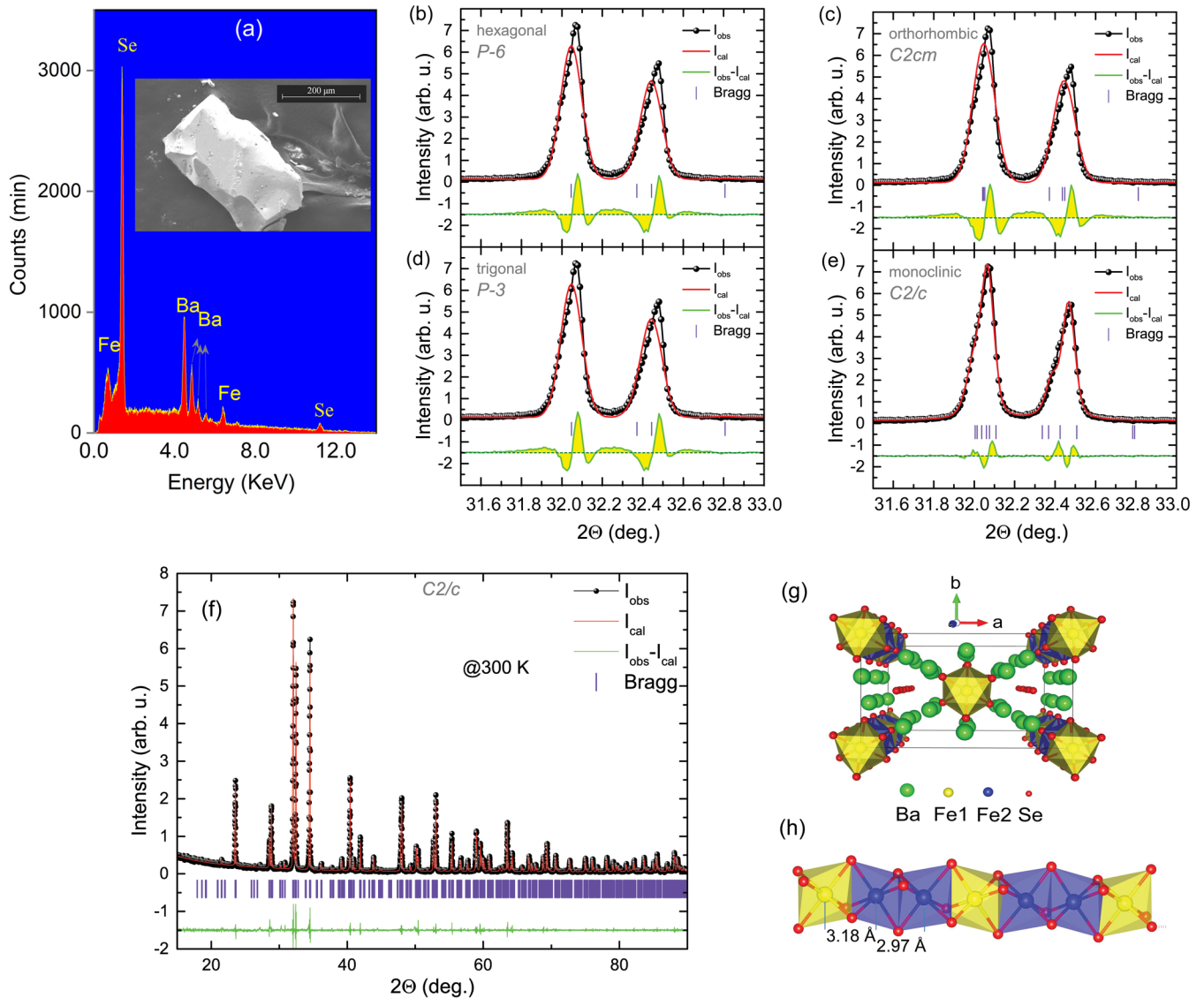


FIG. 1. (a) Energy-dispersive x-ray (EDX) spectroscopy measured for a $Ba_9Fe_3Se_{15}$ single crystal. The inset shows the image of the scanning electronic microscopy for $Ba_9Fe_3Se_{15}$ single crystal. (b)–(e) Rietveld fits of high-resolution powder x-ray diffraction (XRD) patterns of $Ba_9Fe_3Se_{15}$ for different symmetries based on positional parameters obtained by crystal structure solutions based on single-crystal XRD data. Here, a closeup of the two strongest structural reflections is shown. The green lines indicate the difference between observed and calculated intensities (shifted by -1.5 in the y direction). (f) The powder XRD and its refinement using $C2/c$ structure model. (g) The sketch of the crystal structure of $Ba_9Fe_3Se_{15}$ for the top view. (h) The face-sharing $FeSe_6$ octahedral chain. The experiments of EDX and XRD were performed at room temperature.

formalism clearly indicates the lowest Se oxidation states for Se ions within the Se chains. This indicates the presence of Se^{1-} ions within these Se chains, whereas the valences of all the other Se ions within the $FeSe_6$ octahedral chains are distinctly larger (by ~ 0.7 on average) and, thus, indicative of Se^{2-} ions. Finally, the Fe^{2+} oxidation state in $Ba_9Fe_3Se_{15}$ agrees with the appearance of Se^{1-} ions within the Se chains since the 6 Se^{1-} and 9 Se^{2+} ions are in charge balance with the 3 Fe^{2+} and 9 Ba^{2+} ions.

The oxidation state of the iron ions in $Ba_9Fe_3Se_{15}$ has been investigated by soft XAS spectrum at the $Fe-L_{2,3}$ edge, which is very sensitive to the valence state [18,19] and the local environment [20,21]. Figure 2(a) shows the $Fe L_{2,3}$ XAS of $Ba_9Fe_3Se_{15}$ together with those of $Mg_{0.96}Fe_{0.04}O$ as a Fe^{2+}

reference (taken from Ref. [22]) and Fe_2O_3 as a Fe^{3+} reference. The spectrum of $Ba_9Fe_3Se_{15}$ is shifted by >1 eV to lower photon energy relative to that of the Fe_2O_3 but is at the same photon energy as that of $Mg_{0.96}Fe_{0.04}O$, demonstrating the $2+$ valence state for Fe ions in $Ba_9Fe_3Se_{15}$. The oxidation state of iron in $Ba_9Fe_3Se_{15}$ was also confirmed by Mössbauer spectroscopy, see Fig. 2(b). Because there are two Fe sites in $Ba_9Fe_3Se_{15}$, two curves were used to fit for the measured data. The obtained isomer shift (CS) is about 0.91 and 0.92 mm/s for the Fe1 and Fe2 atoms, respectively, which confirms the $2+$ oxidation state observed in the BVS of both Fe atoms as derived from single-crystal XRD. The quadrupole splitting (QP) is 0.78 mm/s for Fe1 and 1.35 mm/s for Fe2. The magnitude of the QP reflects the homogenization of the field

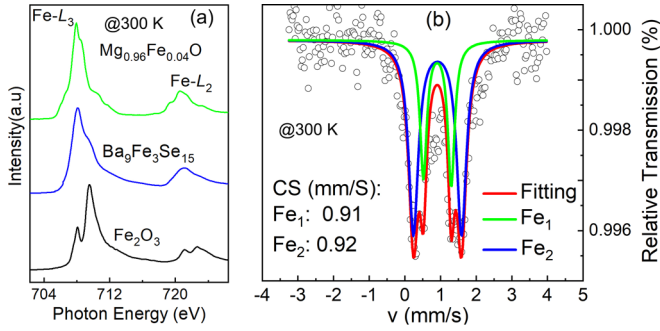


FIG. 2. (a) Fe $L_{2,3}$ x-ray absorption spectra of $\text{Ba}_9\text{Fe}_3\text{Se}_{15}$ and of Fe_2O_3 and $\text{Mg}_{0.96}\text{Fe}_{0.04}\text{O}$ (taken from Ref. [22]) as Fe^{3+} and Fe^{2+} references, respectively; (b) Mössbauer spectroscopy for $\text{Ba}_9\text{Fe}_3\text{Se}_{15}$ with isotope of ^{57}Fe .

around the Fe atoms. The smaller value of the QP of the Fe1 atom indicates that its field is more homogenous than that of the Fe2 atom, which is consistent with the observation of dimerization of two neighboring Fe2 atoms. The dimerization should result in highly asymmetric selenium environments due to the shift of both Fe2 atoms toward the shared face of the two adjacent Se octahedral. In contrast to that, the Fe1 atoms are located almost in the center of their Se octahedral surrounding.

Figure 3(a) shows the temperature dependence of resistivity for the $\text{Ba}_9\text{Fe}_3\text{Se}_{15}$ sample, which exhibits semiconducting behavior. The inset presents the linear fit to the curve of $\ln(\rho)$ as a function of inverse temperature using the formula of $\rho \propto \exp(\Delta_g/2k_B T)$, where Δ_g is the semiconducting band gap and k_B is the Boltzmann's constant. The resistivity curve can be well fitted, and the band gap Δ_g of $\text{Ba}_9\text{Fe}_3\text{Se}_{15}$ is evaluated to be ~ 460 meV, which is larger than $\text{Ba}_9\text{Fe}_3\text{Te}_{15}$ with the data also shown in Fig. 3(a) [15]. Figure 3(b) displays the magnetic susceptibility measured for the polycrystalline sample of $\text{Ba}_9\text{Fe}_3\text{Se}_{15}$ with magnetic field of $H = 100$ Oe. It exhibits a FM-like phase transition at ~ 14 K. The lower inset of Fig. 3(b) is the magnetic hysteresis loop measured at 2 K. The magnetization shows saturation when $H > 500$ Oe. The saturated moment is $\sim 0.7 \mu_B/\text{Fe}$, which is much smaller than that expected for Fe^{2+} with $S = 2$. It suggests that the magnetic phase is ferrimagnetic or canted AFM. The susceptibility in the paramagnetic region deviates from Curie-Weiss behavior within 300 K, as shown in the upper inset of Fig. 3(b), which usually arises from the unquenched orbital moment [23]. Therefore, we conducted a measurement within a higher temperature range of 500–700 K and made a Curie-Weiss fit. The effective moment according to this fit amounts to $\mu_{\text{eff}} \sim 6.4 \mu_B$ per Fe. This value is much larger than the expected value for Fe^{2+} with a high-spin state (HS, $S = 2$), which further indicates that the effective moment should contain orbital contributions.

We now resort to the element selective x-ray magnetic circular dichroism (XMCD) spectroscopy to further study the magnetic property of the Fe ions. An important feature of XMCD experiments is that there are sum rules, which were developed by Thole *et al.* [24] and Carra *et al.* [25], to determine the ratio between the orbital $m_{\text{orb}} = L_z$ and spin

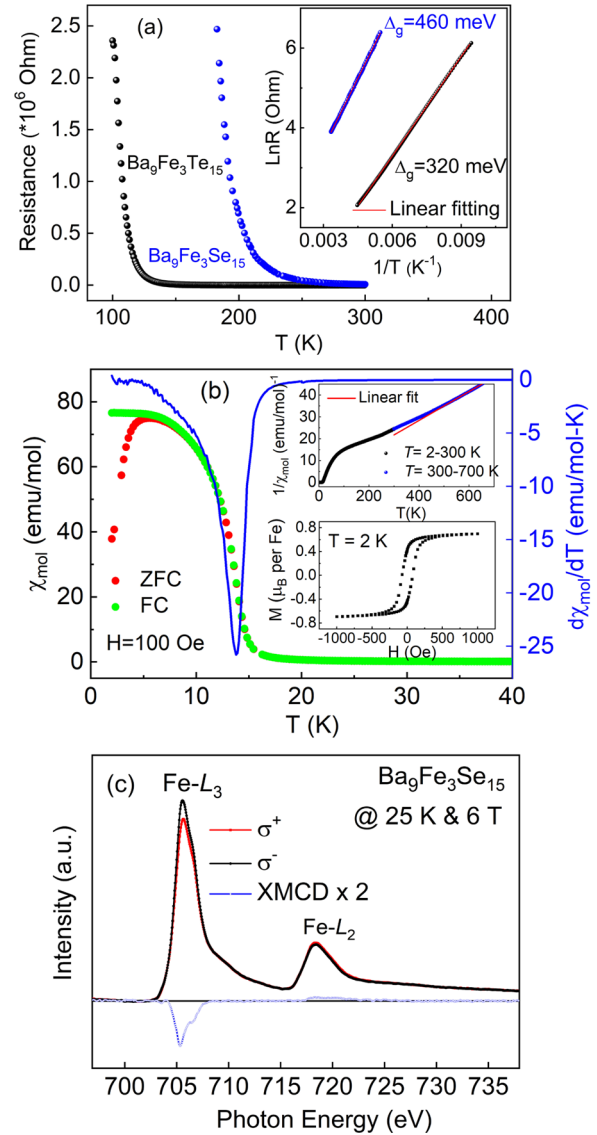


FIG. 3. (a) Temperature dependence of resistivity of $\text{Ba}_9\text{Fe}_3\text{X}_{15}$, $X = \text{Se}$ and Te . The inset is the $\ln(\rho)$ as a function of inverse temperature and its linear fitting. The resistivity data of $X = \text{Te}$ is taken from the reference of Ref. [15]. (b) The susceptibility measured with $H = 100$ Oe and the temperature derivative susceptibility showing the magnetic transition temperature $T_N \sim 14$ K. The upper inset is the inverse susceptibility within the temperature range of 2–700 K, and the lower inset is the magnetic hysteresis loops measured at 2 K. (c) Fe- $L_{2,3}$ x-ray absorption spectra of $\text{Ba}_9\text{Fe}_3\text{Se}_{15}$ taken at 25 K and 6 T using circularly polarized x rays with the photon spin parallel (σ^+ red line) and antiparallel (σ^- black line) to the applied magnetic field, respectively. The difference spectrum x-ray magnetic circular dichroism (XMCD) is shown in blue line.

$m_{\text{spin}} = 2S_z$ contributions to the magnetic moment, namely,

$$\frac{L_z}{2S_z + 7T_z} = \frac{2}{3} \frac{\int_{L_{2,3}} (\sigma^+ - \sigma^-) dE}{\int_{L_3} (\sigma^+ - \sigma^-) dE - 2 \int_{L_2} (\sigma^+ - \sigma^-) dE}, \quad (1)$$

where the σ^+ and σ^- indicate the spectra taken with circularly polarized x rays with the photon spin parallel or antiparallel

to the applied magnetic field, respectively. Here, T_z denotes the magnetic dipole moment. For ions in octahedral symmetry T_z is small and can be neglected compared with S_z [26]. Figure 3(c) shows Fe- $L_{2,3}$ XAS spectra of $\text{Ba}_9\text{Fe}_3\text{Se}_{15}$ taken at 25 K and 6 T using circularly polarized x rays with the photon spin parallel (σ^+ red line) and antiparallel (σ^- black line) to the applied magnetic field, respectively. One can clearly observe large differences between the two spectra. Their difference is the XMCD spectrum (blue).

In this case, we can immediately recognize the presence of a large orbital moment in Fig. 3(c) since there is a large net negative integrated XMCD spectral weight. By using Eq. (1), we find $m_{\text{orb}}/m_{\text{spin}} = 0.35$, and thereby, the orbital moment was calculated to be $\sim 1.4 \mu_B$ if assuming $S = 2$ for HS Fe^{2+} . Using the orbital and spin momentum values, we can calculate the g factor to be ~ 1.58 and then the effective moment $\mu_{\text{eff}} \sim 6.1 \mu_B$ via the equation of $\mu_{\text{eff}} = g\sqrt{J(J+1)}$, where $J = 3.4 \mu_B$ is the sum of L and S . The obtained μ_{eff} from the XMCD experiments agrees well with that from magnetic susceptibility measurement, which confirms the unquenched orbital moment in the system and the assumption of the HS form with $S = 2$. The observation of sizeable orbital moment is quite common in cobalt-based compounds with a HS $3d^6$ ionic configuration in octahedral coordination [27–29]. Also, several iron-based compounds such as FeBr_2 [30,31] and $\text{Ba}_9\text{Fe}_3\text{Te}_{15}$ [15] have been reported to possess unquenched orbital moment.

The properties of $\text{Ba}_9\text{Fe}_3\text{Se}_{15}$ under high-pressure condition was investigated. The *in situ* angle dispersive synchrotron XRD patterns of $\text{Ba}_9\text{Fe}_3\text{Se}_{15}$ were recorded at room temperature to study the structure stability under pressure, as shown in Figs. 4(a)–4(c). Figure 4(a) is the XRD patterns measured under pressure within 51 GPa. All the Bragg peaks shift gradually to the high angle direction as the pressure increases, suggesting the shrink of lattice constants under pressure. No new Bragg peak is observed, which reveals that the crystal structure is stable within the highest experimental pressure. Figure 4(b) presents the pressure dependence of the lattice parameters a , b , and c . These lattice parameters are decreased by $\sim 13.2\%$, $\sim 13.8\%$, and $\sim 16.8\%$ within 51 GPa, respectively. In addition, an anomaly can be clearly seen at ~ 30 GPa for each curve. Since the crystal structure is stable, the anomaly suggests an electronic transition, which will be confirmed by the following experiments. The cell volume as a function of pressure is plotted in Fig. 4(c). Using the Birch-Murnaghan equation of $P(\text{GPa}) = \frac{3}{2}B_0[(\frac{V_0}{V})^{7/3} - (\frac{V_0}{V})^{5/3}] \times \{1 - (3 - \frac{3}{4}B') \times [(\frac{V_0}{V})^{2/3} - 1]\}$ with B' being fixed with 4, the data within 30 GPa are fitted; the bulk modulus $B_0 = 34.7(5)$ GPa is obtained.

For the transition-metal atom, the $K\beta(3p \rightarrow 1s)$ emission line is extremely sensitive to its spin state. Figure 5(a) displays the Fe $K\beta$ XESs of $\text{Ba}_9\text{Fe}_3\text{Se}_{15}$ between ambient pressure and 36 GPa. All the XESs show a main peak called the Fe $K\beta_{1,3}$ spectral line and a satellite peak denoted as the Fe $K\beta'$ line on the lower energy side of Fe $K\beta_{1,3}$. When pressure increases, the intensity of the Fe $K\beta'$ peak becomes weak and almost disappears at 36 GPa. At the same time, its spectral weight is transferred to the main peak of Fe $K\beta_{1,3}$, as can be clearly seen in Fig. 5(b). The very weak Fe $K\beta'$ peak

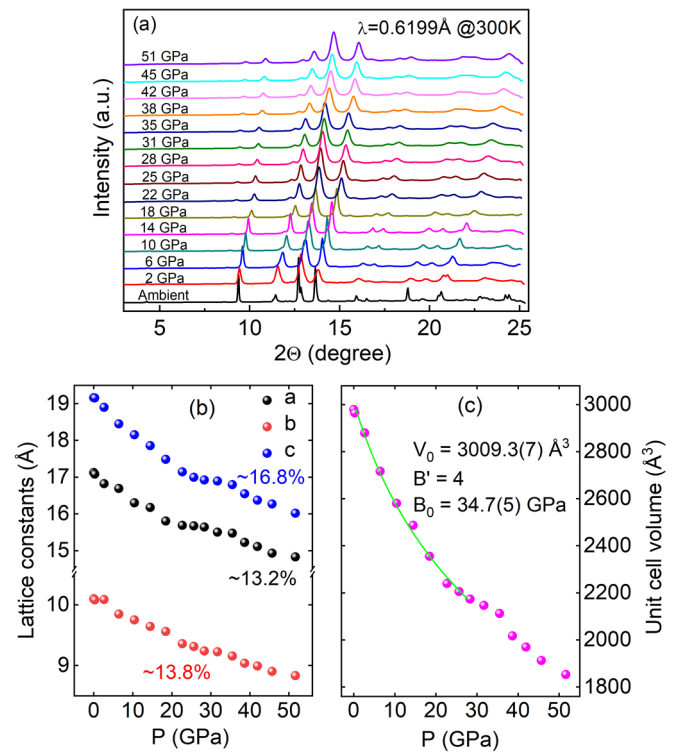


FIG. 4. (a) The synchrotron x-ray diffraction patterns of $\text{Ba}_9\text{Fe}_3\text{Se}_{15}$ measured at room-temperature and high-pressure conditions. (b) The lattice constants a , b , and c as a function of pressure. (c) The pressure dependence of unit volume V . The green solid line is the fitting using the Birch-Murnaghan equation within 30 GPa, where B' is fixed with 4.

indicates a low-spin state (LS, $S \rightarrow 0$) should be reached. The change of spin moment can also be estimated from the integrated absolute difference (IAD) between the Fe $K\beta$ XES. According to the procedure described by Vankó *et al.* [32], the spectra were normalized firstly with respect to the areas and then shifted to centers of mass at the same position. To obtain the IAD, we can use the spectrum taken at the highest experimental pressure of 36 GPa as the reference. Figure 5(b) presents the typical normalized XES of Fe $K\beta$ spectral line taken at 1 GPa and the difference of the spectral intensity. The integrals of the absolute difference under different pressure are presented in Fig. 5(c). At ambient pressure, the value of IAD is obtained to be ~ 0.12 . The IAD value decreases with pressure and drops quickly at 29 GPa, which could be caused by either the enhancement of the crystal field or the delocalization of $3d$ electrons. The following experiments will imply that the metallization plays a predominant role. The pressure dependence of IAD indicates that a SST starts at ~ 29 GPa, which is consistent with the abnormal variation of the lattice parameters under pressure observed in the high-pressure XRD experiments. The value of IAD at ambient pressure is slightly smaller than that of IAD estimated from the XES of HS and 100% LS calculated for FeO [33], which implies that $\text{Ba}_9\text{Fe}_3\text{Se}_{15}$ undergoes a spin transition from HS to LS under high pressure, but not HS to intermediate-spin state.

The high-pressure electronic transport properties of $\text{Ba}_9\text{Fe}_3\text{Se}_{15}$ were investigated as shown in Figs. 6(a) and

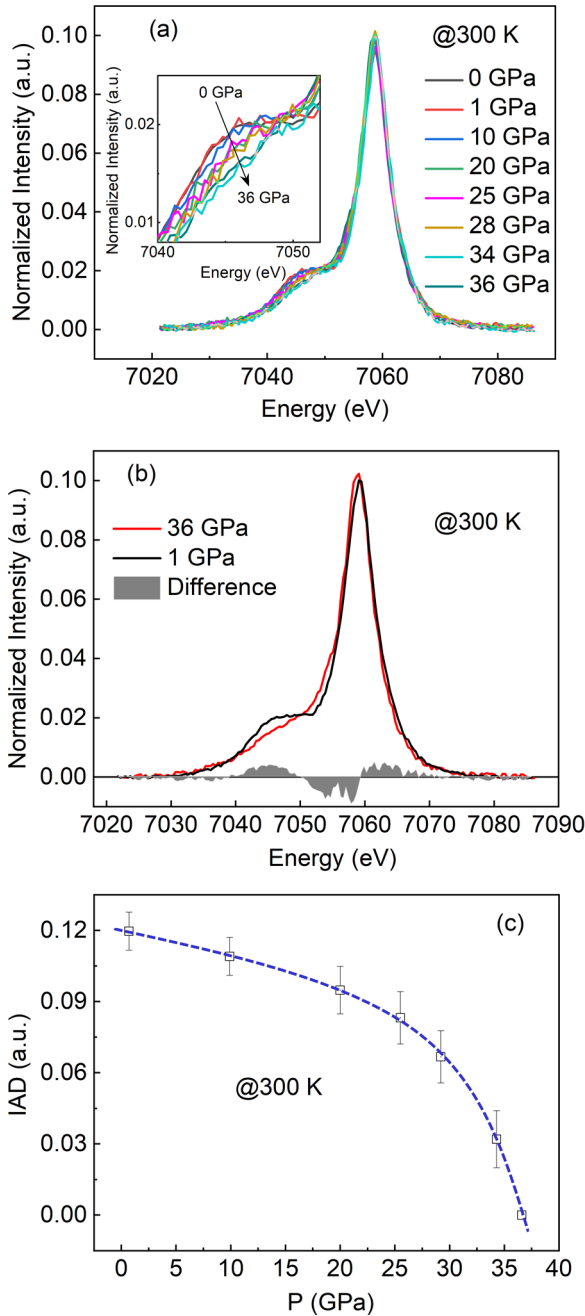


FIG. 5. (a) The x-ray emission spectroscopies of $\text{Ba}_9\text{Fe}_3\text{Se}_{15}$ measured under different pressures at 300 K. (b) The typical normalized x-ray emission spectra (XES) of Fe $K\beta$ spectral line taken at 1 and 36 GPa and their difference of the spectral intensity. (c) The pressure dependence of integrated absolute difference (IAD) value. The XES taken at 36 GPa was used as the reference. The IAD values are obtained by the integration of the absolute difference between the XES and the reference spectrum. The blue dashed line is a guide to the eye.

6(b). The insulating characteristic is gradually suppressed by pressure, and a pressure-induced metallization occurs starting from ~ 21 GPa, where it exhibits metallic behavior at low temperature and undergoes a metal-to-insulator transition (MIT) at ~ 130 K. As pressure increases to 26 GPa, the MIT temperature is enhanced to ~ 250 K. When pressure

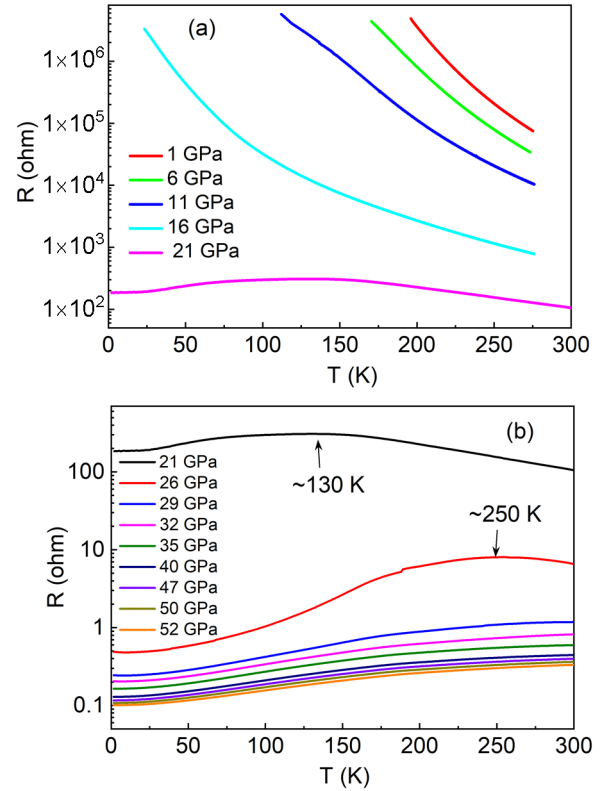


FIG. 6. Temperature dependence of the resistance measured under different applied pressures (a) from 1 to 21 GPa and (b) from 21 to 52 GPa.

> 29 GPa, $\text{Ba}_9\text{Fe}_3\text{Se}_{15}$ exhibits metallic behavior within measured temperature range. Just near the pressure of complete metallization, the IAD value associated with localized spin moments shows a sharp decrease. This hints that the delocalization of the $3d$ electrons causes the spin state crossover from HS to LS. Within the experimental pressure range of 0–51 GPa, no SC is observed.

The discovery of $\text{Ba}_9\text{Fe}_3\text{Se}_{15}$ completes the series of $\text{Ba}_9\text{Fe}_3\text{X}_{15}$ ($X = \text{S}, \text{Se}, \text{Te}$) that consists of face-sharing FeX_6 octahedral chains along the c axis. The partial lattice parameters for $\text{Ba}_9\text{Fe}_3\text{X}_{15}$ are listed in Table II. The data of $\text{Ba}_9\text{Fe}_3\text{Te}_{15}$ and $\text{Ba}_9\text{Fe}_3\text{S}_{15}$ are taken from Refs. [15,17]. For the three compounds, the FeX_6 chains are separated by $> 9 \text{ \AA}$, exhibiting strongly 1D spin-chain structure. The variation of anion from $X = \text{S}$ to Te leads to the increase of bond length Fe-X and average intrachain and interchain distance of Fe-Fe. In fact, in this 1D system,

TABLE II. The partial lattice parameters of $\text{Ba}_9\text{Fe}_3\text{X}_{15}$ ($X = \text{S}, \text{Se}, \text{Te}$). The averaged intrachain distance of Fe-Fe is denoted with d_{intra} that is the lattice constant c divided by six; while the interchain distance of Fe-Fe is denoted with d_{inter} .

Compound	Fe-X bond length	d_{intra}	d_{inter}
$\text{Ba}_9\text{Fe}_3\text{S}_{15}$	2.5120–2.5691 \AA	3.0095 \AA	9.2349 \AA
$\text{Ba}_9\text{Fe}_3\text{Se}_{15}$	2.6359–2.7467 \AA	3.0112 \AA	9.6128 \AA
$\text{Ba}_9\text{Fe}_3\text{Te}_{15}$	2.8094–3.0556 \AA	3.3029 \AA	10.2366 \AA

the enhancement of interchain distance d_{inter} weakens the 1D conducting characteristic, as will be discussed below. In addition, $\text{Ba}_9\text{Fe}_3\text{Se}_{15}$ shows a quasi-1D conducting behavior. Compared with its sister compounds $\text{Ba}_9\text{Fe}_3\text{Te}_{15}$ [15], the band gap of $\text{Ba}_9\text{Fe}_3\text{Se}_{15}$ is enhanced when the anions of Te are replaced by smaller ion size of Se, as seen in the inset of Fig. 3(a). It is in contrast with that in $\text{BaFe}_2\text{S}/\text{Se}_3$, where the band gap was reduced due to the lattice shrink with the substitution of Se by S [7,34]. Indeed, the increase of the band gap in $\text{Ba}_9\text{Fe}_3\text{Se}_{15}$ is a typical phenomenon observed in the system with quasi-1D conducting chains, where the electron hopping t among the chains determines the transport property [35,36]. Since the Se-4*p* electrons are more localized than Te-5*p* ones, the replacement of Te by the smaller size of Se should reduce the electron hopping between FeTe/Se₆ chains and result in an increase of the band gap. Therefore, although the interchain distance of FeX₆ chains decreases when X changes from Te to Se, the 1D conducting characteristic becomes stronger. High pressure can enhance the electron hopping and change the system to a three-dimensional metal. A high-dimensional metallic state will be realized after the interchain electric hopping t exceeds a critical value of t^* . However, the interchain hopping can be masked by the thermal fluctuation as temperature increases, which should lead to a MIT. Therefore, the observation of MIT in $\text{Ba}_9\text{Fe}_3\text{Se}_{15}$ reveals the quasi-1D conducting properties. During the crossover to a three-dimensional metal, the local moment is reduced gradually, and a LS is realized when pressure >36 GPa. In this process, no SC was observed in $\text{Ba}_9\text{Fe}_3\text{Se}_{15}$, which is speculated to be related with the ferromagnetic component in $\text{Ba}_9\text{Fe}_3\text{Se}_{15}$. Generally, SC can be induced via suppressing an AFM order either by charge carrier doping or applying high pressure [37]. For $\text{Ba}_9\text{Fe}_3\text{Te}_{15}$, since the intrachain spin exchange coupling is AFM under ambient pressure, it is possible for $\text{Ba}_9\text{Fe}_3\text{Te}_{15}$ to be a super-

conductor under high pressure [15,16]. However, $\text{Ba}_9\text{Fe}_3\text{Se}_{15}$ has a ferromagnetic component, which might be against the emergence of SC. Besides the quasi-1D conducting behavior, the quasi-1D spin chain structure should give rise to more interesting physical properties associated with magnetism, which deserves to be further studied.

IV. CONCLUSIONS

In conclusion, we synthesized the iron-based compound $\text{Ba}_9\text{Fe}_3\text{Se}_{15}$ under high-pressure and high-temperature conditions. The crystal structure was solved by combining powder and single-crystal XRD measurements. $\text{Ba}_9\text{Fe}_3\text{Se}_{15}$ crystallizes in a monoclinic *C2/c* structure, where the face-sharing FeSe₆ octahedral chains are separated by a distance >9.5 Å. $\text{Ba}_9\text{Fe}_3\text{Se}_{15}$ possesses a FM-like phase transition at ~14 K and has a sizable unquenched orbital moment. It is an insulator with a band gap ~460 meV at ambient pressure. When applying pressure, the metallization starts around ~21 GPa, and a complete metallization is reached for pressures >29 GPa. The pressure-induced SST is related with the delocalization of 3*d* electrons, and a LS state is attained for pressures exceeding 36 GPa.

ACKNOWLEDGMENTS

We thank J. G. Cheng for the help with high-temperature susceptibility experiments. We greatly appreciate the support of the National Key R&D Program of China and the Natural Science Foundation of China under Grants No. 2018YFA0305700, No. 11974410, No. 12004161, No. 11974397, No. 11921004, No. 2017YFA0302900, No. 11820101003, and No. U2032220. We acknowledge the support from the Max Planck POSTECH Hsinchu Center for Complex Phase Materials.

-
- [1] Y. Kamihara, T. Watanabe, M. Hirano, and H. Hosono, *J. Am. Chem. Soc.* **130**, 3296 (2008).
- [2] Z. A. Ren, W. Lu, J. Yang, W. Yi, X. L. Shen, Z. C. Li, G. C. Che, X. L. Dong, L. L. Sun, F. Zhou, and Z. X. Zhao, *Chin. Phys. Lett.* **25**, 2215 (2008).
- [3] M. Rotter, M. Tegel, and D. Johrendt, *Phys. Rev. Lett.* **101**, 107006 (2008).
- [4] X. C. Wang, Q. Q. Liu, Y. X. Lv, W. B. Gao, L. X. Yang, R. C. Yu, F. Y. Li, and C. Q. Jin, *Solid State Commun.* **148**, 538 (2008).
- [5] F. C. Hsu, J. Y. Luo, K. W. Yeh, T. K. Chen, T. W. Huang, P. M. Wu, Y. C. Lee, Y. L. Huang, Y. Y. Chu, D. C. Yan, and M. K. Wu, *Proc. Natl. Acad. Sci. USA* **105**, 14262 (2008).
- [6] H. Takahashi, *Nat. Mater.* **14**, 1008 (2015).
- [7] T. Yamauchi, Y. Hirata, Y. Ueda, and K. Ohgushi, *Phys. Rev. Lett.* **115**, 246402 (2015).
- [8] J. Ying, H. Lei, C. Petrovic, Y. Xiao, and V. V. Struzhkin, *Phys. Rev. B* **95**, 241109(R) (2017).
- [9] Y. Nambu, K. Ohgushi, S. Suzuki, F. Du, M. Avdeev, Y. Uwatoko, K. Munakata, H. Fukazawa, S. Chi, Y. Ueda, and T. J. Sato, *Phys. Rev. B* **85**, 064413 (2012).
- [10] J. Zhang, M. Liu, X. C. Wang, K. Zhao, L. Duan, W. M. Li, J. F. Zhao, L. P. Cao, G. Y. Dai, Z. Deng, S. M. Feng, S. J. Zhang, Q. Q. Liu, Y. F. Yang, and C. Q. Jin, *J. Phys.: Condens. Matter* **30**, 214001 (2018).
- [11] J. Zhang, Y. T. Jia, X. C. Wang, Z. Li, L. Duan, W. M. Li, J. F. Zhao, L. P. Cao, G. Y. Dai, Z. Deng, S. J. Zhang, S. M. Feng, R. Z. Yu, Q. Q. Liu, J. P. Hu, J. L. Zhu, and C. Q. Jin, *NPG Asia Mater.* **11**, 60 (2019).
- [12] L. Duan, X.-C. Wang, J. Zhang, J.-F. Zhao, L.-P. Cao, W.-M. Li, R.-Z. Yu, Z. Deng, and C.-Q. Jin, *Chin. Phys. B* **29**, 036102 (2020).
- [13] L. Duan, X. Wang, F. Zhan, J. Zhang, Z. Hu, J. Zhao, W. Li, L. Cao, Z. Deng, R. Yu, H.-J. Lin, C.-T. Chen, R. Wang, and C. Jin, *Sci. China Mater.* **63**, 1750 (2020).
- [14] T. Murakami, T. Yamamoto, F. Takeiri, K. Nakano, and H. Kageyama, *Inorg. Chem.* **56**, 5041 (2017).
- [15] J. Zhang, L. Duan, Z. Wang, X. C. Wang, J. F. Zhao, M. L. Jin, W. M. Li, C. L. Zhang, L. P. Cao, Z. Deng, Z. W. Hu, S. Agrestini, M. Valvidares, H. J. Lin, C. T. Chen, J. L. Zhu, and C. Q. Jin, *Inorg. Chem.* **59**, 5377 (2020).

- [16] J. Zhang, M. L. Jin, X. Li, X. C. Wang, J. F. Zhao, Y. Liu, L. Duan, W. M. Li, L. P. Cao, B. J. Chen, L. J. Wang, F. Sun, Y. G. Wang, L. X. Yang, Y. M. Xiao, Z. Deng, S. M. Feng, C. Q. Jin, and J. L. Zhu, *Chin. Phys. Lett.* **37**, 087106 (2020).
- [17] J. M. Jenks, J. T. Hoggins, L. E. Rendon, S. Cohen, and H. Steinfink, *Inorg. Chem.* **17**, 1773 (1978).
- [18] T. Burnus, Z. Hu, H. Wu, J. C. Cezar, S. Niitaka, H. Takagi, C. F. Chang, N. B. Brookes, H. J. Lin, L. Y. Jang, A. Tanaka, K. S. Liang, C. T. Chen, and L. H. Tjeng, *Phys. Rev. B* **77**, 205111 (2008).
- [19] N. Hollmann, Z. Hu, M. Valldor, A. Maignan, A. Tanaka, H. H. Hsieh, H. J. Lin, C. T. Chen, and L. H. Tjeng, *Phys. Rev. B* **80**, 085111 (2009).
- [20] J. X. Zhang, Q. He, M. Trassin, W. Luo, D. Yi, M. D. Rossell, P. Yu, L. You, C. H. Wang, C. Y. Kuo, J. T. Heron, Z. Hu, R. J. Zeches, H. J. Lin, A. Tanaka, C. T. Chen, L. H. Tjeng, Y. H. Chu, and R. Ramesh, *Phys. Rev. Lett.* **107**, 147602 (2011).
- [21] C. Y. Kuo, Z. Hu, J. C. Yang, S. C. Liao, Y. L. Huang, R. K. Vasudevan, M. B. Okatan, S. Jesse, S. V. Kalinin, L. Li, H. J. Liu, C. H. Lai, T. W. Pi, S. Agrestini, K. Chen, P. Ohresser, A. Tanaka, L. H. Tjeng, and Y. H. Chu, *Nat. Commun.* **7**, 12712 (2016).
- [22] T. Haupricht, R. Sutarto, M. W. Haverkort, H. Ott, A. Tanaka, H. H. Hsieh, H. J. Lin, C. T. Chen, Z. Hu, and L. H. Tjeng, *Phys. Rev. B* **82**, 035120 (2010).
- [23] J. Kanamori, *Prog. Theor. Phys.* **17**, 177 (1957).
- [24] B. T. Thole, P. Carra, F. Sette, and G. Vanderlaan, *Phys. Rev. Lett.* **68**, 1943 (1992).
- [25] P. Carra, B. T. Thole, M. Altarelli, and X. D. Wang, *Phys. Rev. Lett.* **70**, 694 (1993).
- [26] Y. Teramura, A. Tanaka, and T. Jo, *J. Phys. Soc. Jpn.* **65**, 1053 (1996).
- [27] M. W. Haverkort, Z. Hu, J. C. Cezar, T. Burnus, H. Hartmann, M. Reuther, C. Zobel, T. Lorenz, A. Tanaka, N. B. Brookes, H. H. Hsieh, H. J. Lin, C. T. Chen, and L. H. Tjeng, *Phys. Rev. Lett.* **97**, 176405 (2006).
- [28] S. Agrestini, C. Y. Kuo, D. Mikhailova, K. Chen, P. Ohresser, T. W. Pi, H. Guo, A. C. Komarek, A. Tanaka, Z. Hu, and L. H. Tjeng, *Phys. Rev. B* **95**, 245131 (2017).
- [29] T. Yang, Y. Zhang, S. H. Yang, G. B. Li, M. Xiong, F. H. Liao, and J. H. Lin, *Inorg. Chem.* **47**, 2562 (2008).
- [30] Z. Ropka, R. Michalski, and R. J. Radwanski, *Phys. Rev. B* **63**, 172404 (2001).
- [31] S. J. Youn, B. R. Sahu, and K. S. Kim, *Phys. Rev. B* **65**, 052415 (2002).
- [32] G. Vankó, T. Neisius, G. Molnar, F. Renz, S. Karpati, A. Shukla, and F. M. F. de Groot, *J. Phys. Chem. B* **110**, 11647 (2006).
- [33] A. Mattila, J. P. Rueff, J. Badro, G. Vanko, and A. Shukla, *Phys. Rev. Lett.* **98**, 196404 (2007).
- [34] B. Sapiro, S. Calder, B. Sipos, H. Cao, S. Chi, D. J. Singh, A. D. Christianson, M. D. Lumsden, and A. S. Sefat, *Phys. Rev. B* **84**, 245132 (2011).
- [35] L. Duan, J. Zhang, X. C. Wang, J. F. Zhao, L. P. Cao, W. M. Li, Z. Deng, R. Z. Yu, Z. Li, and C. Q. Jin, *J. Alloys Compd.* **831**, 154697 (2020).
- [36] A. Akrap, V. Stevanovic, M. Herak, M. Miljak, N. Barisic, H. Berger, and L. Forro, *Phys. Rev. B* **78**, 235111 (2008).
- [37] C. W. Chu, *Int. J. Mod. Phys. B* **24**, 4102 (2010).